

# FUSION OF SPATIO-TEMPORAL AND MULTI-SCALE FREQUENCY FEATURES FOR DRY ELECTRODES MI-EEG DECODING

Tianyi Gong<sup>1†</sup>, Can Han<sup>2†</sup>, Junxi Wu<sup>3</sup>, Dahong Qian<sup>2</sup>,

<sup>1</sup> School of Data Science, The Chinese University of Hong Kong, Shenzhen, China

<sup>2</sup> School of Biomedical Engineering, Shanghai Jiao Tong University, Shanghai, China

<sup>3</sup> OYMotion Technology Co., Ltd

122090863@link.cuhk.edu.cn, {hancan, dahong.qian}@sjtu.edu.cn, JCjunxi@gmail.com

## ABSTRACT

Dry-electrode Motor Imagery Electroencephalography (MI-EEG) enables fast, comfortable, real-world Brain Computer Interface by eliminating gels and shortening setup for at-home and wearable use. However, dry recordings pose three main issues: lower Signal-to-Noise Ratio with more baseline drift and sudden transients; weaker and noisier data with poor phase alignment across trials; and bigger variances between sessions. These drawbacks lead to larger data distribution shift, making features less stable for MI-EEG tasks. To address these problems, we introduce STGMFM, a tri-branch framework tailored for dry-electrode MI-EEG, which models complementary spatio-temporal dependencies via dual graph orders, and captures robust envelope dynamics with a multi-scale frequency mixing branch, motivated by the observation that amplitude envelopes are less sensitive to contact variability than instantaneous waveforms. Physiologically meaningful connectivity priors guide learning, and decision-level fusion consolidates a noise-tolerant consensus. On our collected dry-electrode MI-EEG, STGMFM consistently surpasses competitive CNN/Transformer/graph baselines. Codes are available at <https://github.com/Tianyi-325/STGMFM>.

**Index Terms**— Electroencephalography, motor imagery, dry electrodes, graph neural network, frequency mixing

## 1. INTRODUCTION

Non-invasive Electroencephalography (EEG) is the most accessible neural sensing modality for daily-life Brain Computer Interface (BCI) applications. Among non-invasive options, dry-electrode systems avoid conductive gel, shorten setup/cleanup, and better fit out-of-lab use [1, 2]. This practicality directly makes it suitable for rehabilitation at home, longitudinal self-training and wearable assistive interaction, where user comfort, compliance, and scalability are critical. However, dry recordings differ systematically from wet

data: the unstable skin-electrode coupling often elevates and fluctuates impedance, lowering Signal-to-Noise (SNR) and amplifying motion/contact artifacts [1, 2]. Besides, re-positioning across days leads to cross-session drift. What is more, inter-subject variability is exacerbated due to hair and pressure differences. In practice, dry-cap protocols also limit the number and duration of trials to reduce discomfort and time burden, which increases the premium on data-efficient and noise-robust decoding and makes frequent recalibration impractical. Currently, most existing Motor Imagery (MI) decoders were designed/validated under wet-electrode assumptions, and most of them transfer poorly to dry conditions due to the noise characteristics, distribution shift, and trial scarcity [3]. As a result, explicit algorithmic tailoring for dry-electrode MI remains under-explored.

Non-invasive BCIs with dry electrodes ease setup, but they typically suffer lower SNR and contact variability, which depresses MI accuracy and calls for noise-robust, data-efficient models [1, 2, 4]. Classical MI pipelines relied on Common Spatial Pattern/bandpower and linear classifiers or Riemannian geometry on covariances [3, 5–7], while deep CNNs improved end-to-end decoding yet still assume relatively clean, well-calibrated signals [8–13]. Graph formulations encode inter-channel relations and have shown benefits for spatio-temporal fusion and cross-session robustness [14]—most notably ST-GF by Wang *et al.* [15]; multi-branch/domain-generalization schemes further diversify representations via decision fusion [16]. In time-series modeling, recent “mixers” learn multi-period structure with compact, multi-resolution tokenization, including TimeMixer and its successor TimeMixer++ by Wang *et al.* [17, 18], as well as related sequence learners [19, 20]. Connectivity priors such as PLV provide phase-synchrony graphs that are amplitude-invariant and physiologically meaningful [21, 22].

Although these advances are compelling, most were devised and tuned with wet-electrode data rather than dry EEG. Therefore, they fail to remediate the low-SNR, contact-motion-artifact instability. They also emphasize localized patterns and lack multi-view learning, limiting the learning

†These authors contributed to the work equally.

Partially supported by Shanghai AIMIC Medical Electronics Co.

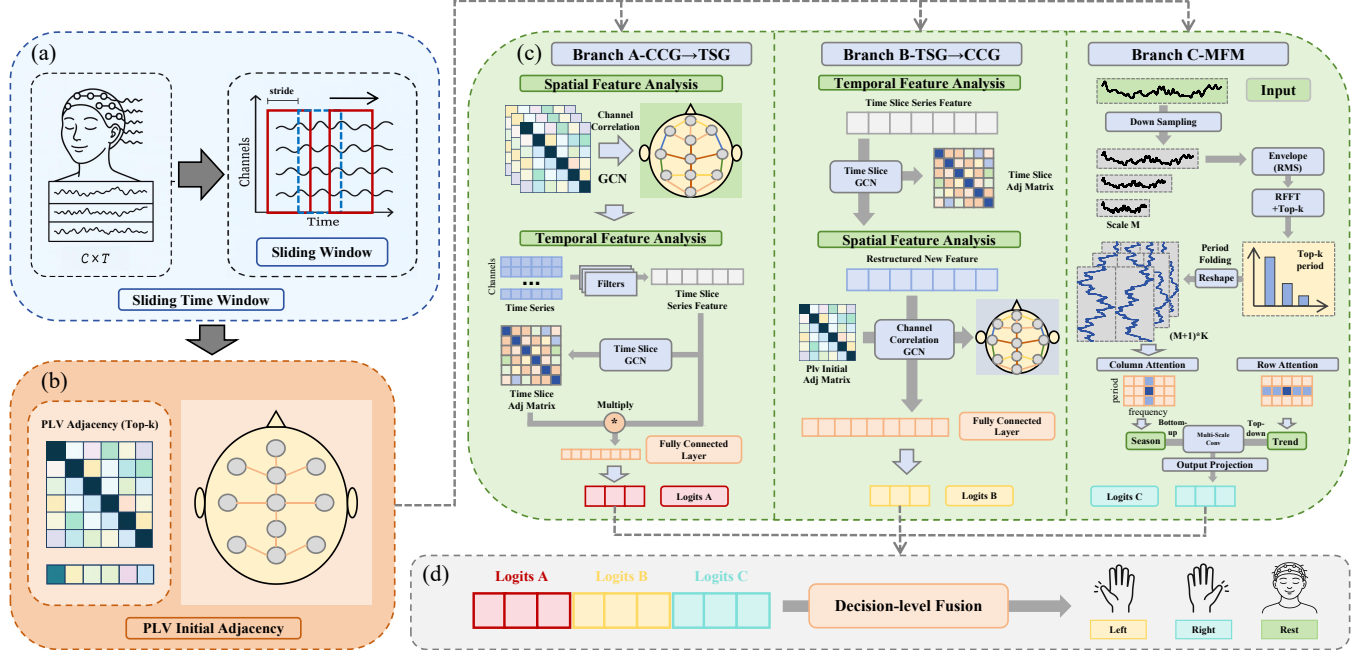


**Fig. 1.** Pipeline of the proposed model. Raw EEG is windowed into overlapping segments and processed by three branches. **A** (CCG→TSG) aligns functional connectivity via a PLV-initialized channel graph before aggregating on a time-slice graph. **B** (TSG→CCG) first reconstructs intra-trial continuity and then fuses channels on the CCG. **C** (MFM) operates on the amplitude envelope (RMS) with multi-resolution imaging and cross-scale mixing. Linear head fuses branch logits at the decision level.

of deep, invariant features to bridge cross-session/subject shifts. In addition, multi-scale spatio and temporal structure is under-explored, leaving deep cross-scale cues untapped. Motivated by these gaps, we propose **STGMFM**, which unifies dual ordered spatio-temporal graph branches (CCG→TSG and TSG→CCG) so that spatial-first and temporal-first propagation can hedge against different noise pathways. And we augment them with a multi-scale frequency mixer that learns multi-resolution envelope dynamics, aligned with ERD/ERS to offer a robust temporal cue when instantaneous waveform detail is unreliable. Physiological connectivity priors (PLV) provide a relatively detailed and precise starting point that is then adapted end-to-end to accommodate subject/session variability, while decision-level fusion forms a simple consensus that resists over-reliance on any single branch. In experiments on a dry-electrode MI-EEG dataset, STGMFM outperforms CNN/transformer/graph baselines, proving it to be a practical path toward dry-electrode BCIs.

**Main contributions:** (1) We introduce a PLV-initialized EEG graph that creates a more detailed and precise prior adjacency, suitable for low-SNR dry recordings. (2) We design a dual-order spatio-temporal graph to yield complementary evidence. (3) We introduce a lightweight Multi-Scale Frequency Mixer that extracts phase-invariant, multi-scale temporal cues aligned with ERD/ERS. (4) We employ a stable training recipe (decision-level fusion, L1/L2 regularization, cosine annealing) that reduces overfitting and over-reliance.

## 2. METHODS

### 2.1. Overview

We present a triple-branch framework for cross-subject MI EEG decoding. Raw trials are segmented with overlapping windows. Branches A/B pair a channel-correlation graph (CCG) and a time-slice graph (TSG) in opposite orders (CCG→TSG vs. TSG→CCG), yielding complementary biases—spatial alignment before temporal aggregation vs. temporal stabilization before spatial fusion. Branch C consumes amplitude envelopes to build a lightweight multi-resolution representation of rhythmic/trend dynamics. Each branch outputs logits, and a shallow head fuses them at the decision level, delivering robust generalization without fragile feature-level alignment. Figure 1 illustrates the overall pipeline.

### 2.2. Notation and Sliding Windowing

Let a trial be  $\mathbf{X} \in \mathbf{R}^{C \times T}$  with  $C$  channels and  $T$  time steps. Using window length  $W_n$  and stride  $\text{Str}$ , the number of windows is

$$W = \left\lfloor \frac{T - W_n}{\text{Str}} \right\rfloor + 1. \quad (1)$$

After segmentation, we obtain a 4-D tensor  $\mathbf{X} \in \mathbf{R}^{N \times W \times C \times T_w}$  for batch size  $N$  and per-window length  $T_w = W_n$ . Win-

dowing provides natural nodes for the TSG and a consistent statistical unit for the graph modules and the envelope branch, avoiding drift on long unsegmented sequences.

### 2.3. PLV-driven Initial Channel Graph

To encode functional connectivity as a prior, we build an initial adjacency from the phase-locking value (PLV). For channels  $i$  and  $j$  with analytic phases  $\phi_i(t)$  and  $\phi_j(t)$ ,

$$\text{PLV}(i, j) = \left| \frac{1}{T} \sum_{t=1}^T e^{i(\phi_i(t) - \phi_j(t))} \right|. \quad (2)$$

We remove self-loops, sparsify by per-row Top- $k$  (or a threshold), symmetrize, and degree-normalize to obtain  $\tilde{\mathbf{A}} = \mathbf{D}^{-1/2} \mathbf{A} \mathbf{D}^{-1/2}$ . The same  $\tilde{\mathbf{A}}$  initializes the CCG in both branches. During training, a small learnable increment adapts  $\tilde{\mathbf{A}}$  to subject-specific variability while retaining interpretability. At the same time, it also provides more detailed and precise adjacency. Fig. 2 shows the before/after learning comparison of adjacency under PLV-initial and the basic spatial-neighborhood prior

### 2.4. Branch A: CCG→TSG

Branch A first performs graph propagation on the channel graph to align truly cooperating electrodes and suppress mismatched ones. With node features  $\mathbf{H}^{(l)} \in \mathbf{R}^{C \times d}$ , one CCG layer reads

$$\mathbf{H}^{(l+1)} = \sigma(\tilde{\mathbf{A}} \mathbf{H}^{(l)} \mathbf{W}_s^{(l)}), \quad l = 0, \dots, K_s - 1. \quad (3)$$

We visualized the changes in spatial connectivity before and after learning, see Fig. 2. The resulting spatially denoised representation then passes through a shared temporal convolutional block (depthwise-pointwise 1D convolution with GELU/normalization) and is aggregated over the *time-slice graph*. Let  $\mathbf{U}^{(l)} \in \mathbf{R}^{W \times d}$  be slice-level features and  $\tilde{\mathbf{S}} \in \mathbf{R}^{W \times W}$  the learnable slice adjacency; one TSG layer is

$$\mathbf{U}^{(l+1)} = \sigma(\tilde{\mathbf{S}} \mathbf{U}^{(l)} \mathbf{W}_t^{(l)}), \quad l = 0, \dots, K_t - 1. \quad (4)$$

Placing temporal aggregation on top of a connectivity-aligned representation improves the SNR of time reconstruction by reducing sensitivity to phase misalignment across channels. A global average pooling (GAP) and a linear head yield  $\mathbf{z}_A$ . We insert a lightweight shared temporal block between CCG and TSG to align feature spaces and add local temporal expressiveness without disturbing the graph inductive bias.

### 2.5. Branch B: TSG→CCG

Branch B starts by reconstructing intra-trial continuity on the slice graph. Continuous MI segments become tightly clustered while non-task fragments are attenuated. The graph-filtered features are then rearranged to the channel dimension

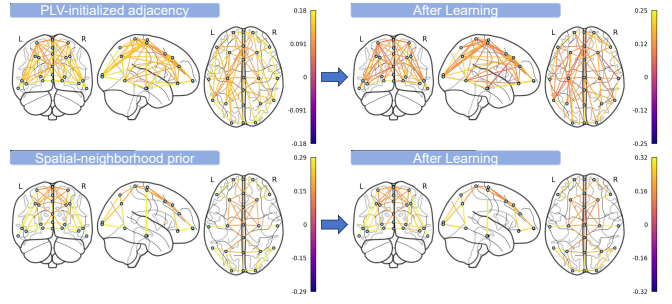


**Fig. 2.** Before/after training comparison of adjacency under two priors: PLV initialization and the spatial-neighborhood prior

and passed through the CCG propagation with  $\tilde{\mathbf{A}}$ . By stabilizing time first, B prevents short-term temporal noise from being prematurely diffused spatially. A shared temporal block and classifier head produce  $\mathbf{z}_B$ . Shared temporal block is also placed between TSG and CCG.

### 2.6. Branch C: Multi-Scale Frequency Mixer

The third branch operates on the amplitude envelope (RMS) (e.g.,  $\mu/\beta$  band), which makes ERD/ERS modulation explicit and phase-invariant. We first form multi-resolution “time images” by selecting dominant periods/frequencies (rfft) and mapping the 1D signal to a compact time–frequency lattice. We then decouple periodic (seasonal) patterns from slower trend evolution using dual-axis processing, and finally carry out multi-scale and multi-resolution mixing to aggregate evidence. This imaging–decoupling–mixing pipeline turns long dependencies into local ones on the image plane and yields a compact cross-scale representation. A lightweight configuration (small channel width and a single block, with one down-sampling and Top-1 dominant period) suits the low-sample EEG regime. The branch outputs  $\mathbf{z}_C$ .

### 2.7. Decision-level Fusion

Let  $[\cdot; \cdot]$  denote concatenation. We fuse logits with a shallow linear head,

$$\mathbf{z} = \mathbf{W}[\mathbf{z}_A; \mathbf{z}_B; \mathbf{z}_C] + \mathbf{b}, \quad \hat{y} = \arg \max_k \mathbf{z}_A. \quad (5)$$

We avoid gating/temperature mechanisms: in small EEG datasets they introduce extra degrees of freedom that are hard to calibrate across subjects and can overfit. A fixed linear combiner preserves class-wise alignment ability while remaining stable.

### 2.8. Objective and Optimization

We train with cross-entropy and combine  $\ell_1$  sparsity on graph-increment parameters with  $\ell_2$  weight decay (AdamW).

**Table 1.** Avg $\pm$ Std results on dry-EEG under three evaluation protocols. We report Accuracy (ACC), Cohen’s kappa, and F1.

Method	Cross Session			Cross Subject			Cross-Subject + Single-Session Fine-tuning		
	ACC(%)	kappa	F1(%)	ACC(%)	kappa	F1(%)	ACC(%)	kappa	F1(%)
ShallowNet [9]	47.30 $\pm$ 7.68	0.2095 $\pm$ 0.1154	45.39 $\pm$ 7.85	50.38 $\pm$ 10.92	0.2621 $\pm$ 0.1643	48.55 $\pm$ 12.13	52.06 $\pm$ 11.30	0.2809 $\pm$ 0.1695	50.18 $\pm$ 12.03
EEGNet [8]	47.67 $\pm$ 11.78	0.2152 $\pm$ 0.1767	45.96 $\pm$ 12.41	52.21 $\pm$ 10.81	0.2936 $\pm$ 0.1625	50.17 $\pm$ 11.85	54.94 $\pm$ 10.23	0.3241 $\pm$ 0.1535	52.71 $\pm$ 11.62
EEG-TCNet [11]	44.52 $\pm$ 11.86	0.1678 $\pm$ 0.1779	40.53 $\pm$ 13.40	46.25 $\pm$ 10.71	0.1936 $\pm$ 0.1415	41.65 $\pm$ 11.26	52.66 $\pm$ 9.12	0.2899 $\pm$ 0.1368	48.15 $\pm$ 11.36
EEGConformer [12]	48.55 $\pm$ 8.62	0.2282 $\pm$ 0.1295	46.07 $\pm$ 9.62	50.23 $\pm$ 9.61	0.2534 $\pm$ 0.1441	48.01 $\pm$ 10.81	55.83 $\pm$ 11.64	0.3374 $\pm$ 0.1746	53.82 $\pm$ 12.81
BaseNet [23]	46.07 $\pm$ 11.16	0.1911 $\pm$ 0.1674	41.80 $\pm$ 13.52	52.05 $\pm$ 10.21	0.2960 $\pm$ 0.1535	48.59 $\pm$ 12.55	53.97 $\pm$ 10.22	0.3095 $\pm$ 0.1534	50.14 $\pm$ 12.05
LMDANet [13]	46.13 $\pm$ 10.70	0.1920 $\pm$ 0.1604	43.58 $\pm$ 11.58	47.89 $\pm$ 8.87	0.2184 $\pm$ 0.1333	45.78 $\pm$ 10.46	51.33 $\pm$ 11.26	0.2701 $\pm$ 0.1689	49.03 $\pm$ 12.17
STGENet [15]	47.08 $\pm$ 10.58	0.2034 $\pm$ 0.1602	43.01 $\pm$ 12.60	47.66 $\pm$ 8.70	0.2155 $\pm$ 0.1253	44.96 $\pm$ 9.63	50.83 $\pm$ 10.28	0.2604 $\pm$ 0.1552	48.75 $\pm$ 11.21
<b>STGMFM</b>	<b>49.25 <math>\pm</math> 4.16</b>	<b>0.2368 <math>\pm</math> 0.0643</b>	<b>47.50 <math>\pm</math> 5.16</b>	<b>57.26 <math>\pm</math> 8.34</b>	<b>0.3592 <math>\pm</math> 0.1247</b>	<b>56.52 <math>\pm</math> 8.08</b>	<b>59.81 <math>\pm</math> 6.71</b>	<b>0.3972 <math>\pm</math> 0.1006</b>	<b>59.22 <math>\pm</math> 6.72</b>

The total loss is

$$\mathcal{L} = \mathcal{L}_{CE} + \lambda_s \|\Delta \tilde{\mathbf{A}}\|_1 + \lambda_t \|\Delta \tilde{\mathbf{S}}\|_1 + \beta \sum_{\theta} \|\theta\|_2^2. \quad (6)$$

Cosine-annealed learning rates promote smooth convergence and better generalization.

### 3. EXPERIMENTS AND RESULTS

#### 3.1. Dataset and Protocols

We collected a dry-electrode MI-EEG dataset with a 23-channel cap at 250 Hz. 19 subjects each completed two sessions on different days; within each session, three repeated runs were recorded for a three-class MI task. We evaluate three realistic protocols: (i) **Cross-Session**: train on one session and test on the other session from the same subject; (ii) **Cross-Subject**: leave one subject out for testing, train on the remaining subjects; (iii) **Cross-Subject + Single-Session Fine-tuning**: pre-train on other subjects and adapt using one session of the target subject. Trials are segmented using windows of 125 samples (0.5 s) with a stride of 125, yielding nine time slices per trial. We train 1000 epochs with AdamW (initial learning rate  $2 \times 10^{-3}$ ), batch size 32, dropout 0.2, cosine-annealing schedule, and L1/L2 regularization on graph weights and classifier. All experiments run on a NVIDIA RTX 4090.

#### 3.2. Baselines and Overall Performance

We compare against some representative models ( ShallowNet [9], EEGNet [8], EEG-TCNet [11], EEGConformer [12], BaseNet [23], LMDANet [13], STGENet [15].) We report 3 averaged metrics over 19 subjects: Accuracy, Cohen’s kappa and F1. Table 1 summarize the results. STGMFM attains the best accuracy across all three protocols.

#### 3.3. Ablation and Component Analysis (on Cross-Subject)

We quantify the contribution of each component using the Cross-Subject protocol. Table 2 reports the results.

**Modules Analysis:** (i) *Dual graph orders* (A: CCG $\rightarrow$ TSG; B: TSG $\rightarrow$ CCG): The two orders inject complementary inductive biases that hedge against distinct error pathways

**Table 2.** Ablation study on dry-EEG under Cross Subject. We report Avg $\pm$ Std results for Accuracy (ACC), Cohen’s kappa, and F1. Best results are **bold**.

Variant	ACC(%)	kappa	F1(%)
Only A&B	54.19 $\pm$ 8.87	0.3132 $\pm$ 0.1327	53.53 $\pm$ 8.78
Only C	51.14 $\pm$ 9.16	0.2669 $\pm$ 0.1376	50.11 $\pm$ 9.45
No PLV initialization	56.76 $\pm$ 8.71	0.3517 $\pm$ 0.1278	56.11 $\pm$ 9.03
Spatial adjacency fixed	52.20 $\pm$ 9.48	0.2834 $\pm$ 0.1420	51.64 $\pm$ 9.50
No L1/L2 regularization	54.32 $\pm$ 9.46	0.3153 $\pm$ 0.1416	53.56 $\pm$ 9.38
Gated fusion	52.89 $\pm$ 9.43	0.2936 $\pm$ 0.1412	52.22 $\pm$ 9.35
<b>STGMFM (full)</b>	<b>57.26 <math>\pm</math> 8.34</b>	<b>0.3592 <math>\pm</math> 0.1247</b>	<b>56.52 <math>\pm</math> 8.08</b>

in dry-EEG: A first stabilizes spatial connectivity then consolidates temporal relations while B emphasizes slice-wise temporal consistency. (ii) *Multi-Scale Frequency-Mixer (C)*: MFM focuses on multi-scale envelopes and long-range modulations with reduced phase sensitivity, recovering ERD/ERS-like patterns that are blurred by dry-electrode noise. (iii) *PLV-initialized, learnable graphs*: PLV provides physiologically plausible priors that narrow the search space and improve early-epoch stability, yet learnability preserves subject/session adaptability. At the same time, it also provides more detailed and precise adjacency. (iv) *Regularization and simple fusion*: L1 prevents spurious edges/feature dominance, while L2 and cosine annealing smooth optimization.

### 4. CONCLUSION

We introduced STGMFM, a tri-branch fusion network for dry-electrode MI-EEG. Two complementary graph orders (CCG $\rightarrow$ TSG and TSG $\rightarrow$ CCG) and a Multi-Scale Frequency-Mixer jointly model spatio-temporal dependencies and envelope regularities. With PLV-initialized learnable graphs, cosine-annealed training, and L1/L2 regularization, STGMFM surpasses strong CNN/Transformer/GCN baselines across cross-session, cross-subject, and pre-train & adapt protocols on a 23-channel dry-EEG dataset. Ablations confirm the role of each module under low-SNR, contact variability: dual graph orders curb noise propagation, MFM captures robust ERD/ERS-like envelopes, and simple decision-level fusion generalizes better than gated schemes. Future work will explore adaptive PLV estimation, subject-aware fusion, and channel pruning for on-device inference.

## 5. REFERENCES

[1] Miguel A. Lopez-Gordo, Daniel Sanchez-Morillo, and Francisco Valle Pineda, “Dry eeg electrodes,” *Sensors*, vol. 14, no. 7, pp. 12847–12870, 2014.

[2] Tony S. Grummets, Roy E. Leibbrandt, Timothy W. Lewis, Daniel DeLosAngeles, David M. Powers, John O. Willoughby, and Kenneth J. Pope, “Validity of artifact-limited eeg data from dry electrodes,” *Clinical Neurophysiology*, vol. 126, no. 3, pp. 556–563, 2015.

[3] Fabien Lotte, Laurent Bougrain, Andrzej Cichocki, et al., “A review of classification algorithms for eeg-based brain–computer interfaces: a 10-year update,” *Journal of Neural Engineering*, vol. 15, no. 3, pp. 031005, 2018.

[4] Keun-Tae Kim, Jaehyung Lee, and Song Joo Lee, “Convolutional neural network approach for mi and ssep-based hybrid bci using dry electrodes,” *Biomedical Signal Processing and Control*, vol. 110, pp. 108343, 2025.

[5] Herbert Ramoser, Johannes Müller-Gerking, and Gert Pfurtscheller, “Optimal spatial filtering of single trial eeg during imagined hand movement,” *IEEE Transactions on Rehabilitation Engineering*, vol. 8, no. 4, pp. 441–446, 2000.

[6] Kai Keng Ang, Zhuoyi Chin, Haihong Zhang, and Cuntai Guan, “Filter bank common spatial pattern (FBCSP) in brain–computer interface,” in *IEEE IJCNN*, 2008, pp. 2390–2397.

[7] Alexandre Barachant, Stéphane Bonnet, Marco Congedo, and Christian Jutten, “Classification of covariance matrices using a riemannian-based kernel for bci applications,” in *Int'l Conf. on Neural Engineering*, 2013, pp. 204–207.

[8] Vernon J. Lawhern, Amelia J. Solon, Nicholas R. Waytowich, Stephen M. Gordon, Chou P. Hung, and Brent J. Lance, “Eegnet: a compact convolutional neural network for eeg-based brain–computer interfaces,” *Journal of Neural Engineering*, vol. 15, no. 5, pp. 056013, 2018.

[9] Robin Tibor Schirrmeister, Jost Tobias Springenberg, Lukas Dominik Fiederer, et al., “Deep learning with convolutional neural networks for eeg decoding and visualization,” in *Human Brain Mapping*, 2017.

[10] Can Han, Chen Liu, Yaqi Wang, Crystal Cai, Jun Wang, and Dahong Qian, “A spatial-spectral and temporal dual prototype network for motor imagery brain-computer interface,” *arXiv preprint arXiv:2407.03177*, 2024.

[11] Trausti Magnus Ingolfsson, Michael Hersche, Luca Benini, and Abbas Rahimi, “Eeg-tcnet: An accurate temporal convolutional network for embedded motor-imagery brain-machine interfaces,” *arXiv preprint arXiv:2006.00622*, 2020.

[12] Y. Song, Q. Zheng, B. Liu, et al., “Eeg conformer: Convolutional transformer for eeg decoding and visualization,” *IEEE Transactions on Neural Systems and Rehabilitation Engineering*, 2022.

[13] Zhaojie Miao, Ziyi Wang, Peiying Xiong, et al., “Lmdanet: A lightweight multi-dimensional attention network for eeg decoding,” *NeuroImage*, 2023.

[14] T. Zhang, X. Chen, and Y. Wang, “Spatio-temporal graph convolutional networks for eeg decoding,” in *ICASSP*, 2022.

[15] Xuhui Wang, Sigang Yu, Kui Zhao, Geng Chen, Enze Shi, and Shu Zhang, “Graph-based fusion of spatial and temporal features for eeg motor imagery decoding,” in *IEEE BIBM*, 2024.

[16] Y. Du et al., “Multi-view ensemble learning for eeg motor imagery classification,” in *ICASSP*, 2023.

[17] Shiyu Wang, Haixu Wu, Xiaoming Shi, Tengge Hu, Huakun Luo, Lintao Ma, James Y. Zhang, and Jun Zhou, “Timemixer: Decomposable multiscale mixing for time series forecasting,” in *Int'l Conf. on Learning Representations (ICLR)*, 2024.

[18] Yue Wang, Zhenyi He, Chang Zhou, Mohammed A. AlZain, Ferrari Dacrema, Jiao Zhang, Zuozhu Liu, Hao Chen, Qiang Zhang, Jian Tang, Li Erran Li, and Hao Wang, “Timemixer++: A general time series pattern machine for universal predictive analysis,” in *Int'l Conf. on Learning Representations (ICLR)*, 2025.

[19] Y. Nie et al., “Patchtst: A patch-mixing transformer for time series,” in *ICLR*, 2023.

[20] Haixu Wu et al., “Timesnet: Temporal 2d-variation modeling for general time series analysis,” in *ICLR*, 2023.

[21] Jean-Philippe Lachaux, Eugenio Rodriguez, Jacques Martinerie, and Francisco J. Varela, “Measuring phase synchrony in brain signals,” *Human Brain Mapping*, vol. 8, no. 4, pp. 194–208, 1999.

[22] H. Kang, C. Dong, Y. Ye, et al., “Plv-guided graph convolutional network with lstm for mi-eeg classification,” *Biomedical Signal Processing and Control*, 2026.

[23] Martin Wimpff, Leonardo Gizzi, Jan Zerfowski, and Bin Yang, “Eeg motor imagery decoding: A framework for comparative analysis with channel attention mechanisms,” *arXiv preprint arXiv:2310.11198*, 2023.